

Supplemental Materials for

Engineering reaction-diffusion networks with properties of neural tissue

Thomas Litschel, Michael M. Norton, Vardges Tserunyan and Seth Fraden

The PDF file includes:

Materials and Methods	2
Experimental Details	5
Simulations	7
Supplementary Figures	9
Supplementary Tables	20
Supplementary Movies	22
Supplementary References	24

Materials and Methods

Fabrication of photoresist master

Photoresist masters for casting the final PDMS device are created with standard photolithography methods. Briefly, we spin coat SU-8 negative photoresist (MicroChem SU-8 2075) on a silicon wafer, soft-bake the photoresist prior to the UV light exposure, place and align a photomask with the desired features on the photoresist, UV-expose the photoresist, hard bake the photoresist, and develop the master with propylene glycol methyl ether acetate. We design the photomasks using Autodesk AutoCAD® and the masks are printed commercially (CAD/Art Services, Inc.). In devices with channels, we use two-height features to make interconnecting channels with lower heights than the wells. This requires two layers of photoresist, which were aligned using alignment-markers and partial development.¹ The schematic in Fig. S9A shows photomask, the silicon-photoresist master and the final PDMS chip (see next section).

Fabrication of PDMS microfluidics

A schematic of the fabrication setup is shown in Fig. S1A and a video of the fabrication process is shown in Movie S6. We mix 10 - 15 g of PDMS (Dow Corning SYLGARD® 184 Silicone Elastomer Kit) with a centrifugal mixer (Thinky® planetary non-vacuum centrifugal mixer). Before applying the PDMS to the silicon-photoresist master, we coat the master with Cytop® CTX-109AE at a dilution 1:40 for 5 seconds. Cytop® is an amorphous fluoropolymer which is used as a mold release agent and is essential for separating the PDMS and photoresist. We place the silicon-photoresist master in a desiccator and pour a small amount of PDMS (just enough to cover the microfluidic features) onto the master. We de-gas the PDMS in the desiccator for 10 minutes until the PDMS is bubble-free. Two 25 mm x 75 mm glass slides are plasma cleaned (plasma cleaner: Diener Zepto) and put onto the PDMS. We then place the setup onto a flat surface and cover it with a sheet of Mylar® to facilitate disassembly after curing. We place two

more glass slides orthogonally to the carrier glasses on the stack. A lead weight of 15 kg is placed onto these glass slides. We let the PDMS cure for 12 hours at room temperature before replacing the heavy weight with a lighter weight and put the entire setup in a 70°C oven for another 6 hours. After curing, the setup is carefully disassembled. The master can be reused without re-applying Cytop®. The final microfluidic device is shown in Fig. S9B.

BZ composition

We use a photosensitive version of the Belousov-Zhabotinsky reaction that employs malonic acid as the organic substrate, ferroin redox indicator as a metal catalyst, and $[\text{Ru}(\text{bpy})_3]^{2+}$ as a photosensitive co-catalyst. Other components of the reaction are sulfuric acid, sodium bromide and sodium bromate. The final BZ solution contains the following chemicals in the given concentrations: Ferroin (3 mM), sodium bromide (25 mM), malonic acid (400 mM), sulfuric acid (80 mM), sodium bromate (288 mM) and $[\text{Ru}(\text{bpy})_3]\text{Cl}_2$ (1.2 mM). The components are mixed in the same order as they appear here. Stock concentrations can be found in Table S1.

Experimental protocol

To maintain BZ oscillations for several hours and to achieve the desired coupling, the microfluidic wells must be properly sealed. The BZ reaction generates CO_2 gas that will create bubbles if open to air. Therefore, we seal the BZ solution air tight with no air bubbles in the wells so that the CO_2 gas remains dissolved in solution. Additionally, we seal the device to prevent the contents of the array of wells to come into contact with each other and with the BZ in the moat used to establish boundary conditions. To achieve these requirements, we designed a clamping device, which isolates the desired volume from air by a glass lid and applies pressure in a way that all wells are evenly sealed. The device consists of a bottom and top clamp frame that has been laser cut from Plexiglas plates. A rubber O-ring encloses an additional reservoir of BZ solution surrounding the sealed area to diminish concentration gradients and diffusion from

the inside through the PDMS. The PDMS wells are sealed by a 3.2 mm x 3.2 mm x 1.7 mm glass window attached to a 25 mm x 25 mm x 1.2 mm glass slide. A round 10 mm in diameter and 3 mm in height PDMS window attached to another 25 mm x 25 mm glass slide allows for even pressure applied directly over the sample. This is important as otherwise the glass bends and lifts off the surface of the wells by a few microns, which is enough space to generate leaks. The entire setup is shown in Fig. S1B.

Before the BZ solution is loaded onto the PDMS chip, the chip is plasma treated in order to functionalize the PDMS surface and render it hydrophilic. Skipping this step prevents BZ solution from properly filling the wells due to the small size of the wells, the hydrophobicity of PDMS and the surface tension of the aqueous solution. We mix the 6 reagents of the BZ reaction together in aqueous solution and immediately pipette the solution onto an array of wells. We then place the setup into our clamp, and the device is tightened under a microscope so that a slight degree of compression is visible, which facilitates proper sealing. Before we start video recording, we wait for 30 to 40 minutes. This has shown to be crucial when choosing high initial concentrations of sodium bromide, since premature sample illumination can prevent oscillations from occurring. The process is shown in Movie S7.

Programmed illumination and recording

For our experiments, we use a homemade programmable illumination microscope.² Its main component is a commercial three-color liquid-crystal display (LCD) projector with the optics inverted so that it reduces the image instead of expanding it as intended by the manufacturer. The computer projector is controlled by MATLAB code that is able to project light onto individual wells to control BZ oscillations by light inhibition.² To illuminate the sample for recording, we use a uniform Köhler illumination with a cyan LED and a green filter that filters light of a wavelength of 510 ± 10 nm. Green light marginally excites $[\text{Ru}(\text{bpy})_3]^{2+}$, but is well suited to

distinguish the two states of the BZ reaction.³ When imaged with a black-and-white CCD camera, the BZ solution appears bright in its oxidized state (blue) and dark in the reduced state (red).

Experimental Details

Experiments to quantify wave speed in dependency of channel size (Fig. 4, Fig. 5, Fig. 6)

The experiments shown in Fig. 4, 5 and 6 and Movies S1 and S3 use a one-dimensional array of wells with a moat-like structure surrounding the array. The “moat” provides defined boundary conditions, as illustrated in Fig. 3A. At the same time, we use the moat to calibrate the light intensity. As shown in Fig. 3B, we use light to create pacemaker wells. We shine the same intensity of light on all BZ compartments, including the moat, except for a single well at the end of the 1D array of wells. Within a small range of light intensities, the BZ solution in the surrounding moat will not oscillate, but we can observe waves traveling through the entire array of wells, originating at the pacemaker well.

It is important to note that if we omit the light inhibition, in many cases unidirectional waves still emerge. Fig. S4B shows the results of an experiment in which only the moat is light-inhibited, but not the one-dimensional arrays. Similar to the light controlled case (Fig. S4A), there is a clear dependence of wave speed on geometry. The propagation speed in the continuous compartment is about double the speed compared to that of the other arrays. Note that the propagation speed values in Fig. S4B are about three times as high as in the light controlled equivalents (Fig. S4A). However, these experiments without pacemaker wells are not reliably reproducible. Fig. S4 (C and D) show period times for both types of experiments.

While the wave speed is relatively constant over time, Fig. S4 (E and F) shows it is not constant across space within traveling waves. Close to the boundaries of the array (the beginning and the end of the array), we observe an increased propagation speed in experiment and simulation.

All experiments use an array of fifteen $100\ \mu\text{m} \times 100\ \mu\text{m} \times 110\ \mu\text{m}$ (L x W x H) wells connected by channels that are $50\ \mu\text{m}$ long. The channels connecting the wells in the experiment shown in Fig. 4, Fig. 5 and Movie S1 are $20\ \mu\text{m}$ wide and $52\ \mu\text{m}$ deep. The continuous chamber is $100\ \mu\text{m}$ wide, $2200\ \mu\text{m}$ long and $110\ \mu\text{m}$ deep. In the experiment shown in Fig. 6 (B and C)

and Movie S3 channels are 20 μm wide and 34 μm deep. In all experiments the moat is 150 μm wide and separated from the linear arrays by 80 μm of PDMS.

Bioinspired central pattern generators (Fig. 8)

The experimental procedure is similar to the procedure for the experiments in Fig. 4 to 6. Instead of having a single pacemaker well, here we have two uninhibited pacemaker wells, located next to each other at one end of each column with excitatory links. To assure in-phase starting conditions, we initially shine light on all wells for the duration of about one BZ oscillation period, which is of order 300 seconds. All wells are 120 μm x 80 μm x 90 μm (L x W x H). Connecting channels are 50 μm long, 20 μm wide and 40 μm deep. The moat is 150 μm wide. 70 μm of PDMS separates moat and the arrays.

Simulations

We model the BZ reaction using the Field-Körös-Noyes (FKN) model.⁴ The model tracks the evolution of six key chemical intermediates of the BZ cycle (bromous acid x , bromide y , oxidized catalyst z , bromine dioxide radical w , hypobromous acid p) and assumes that the feed stocks of the reaction (bromate a , malonic acid m , proton concentration h , and bromomalonic acid b) remain constant.

$$\begin{aligned}
 \frac{dx}{dt} &= -k_1xy + k_2y - 2k_3x^2 - k_4x + k_rw^2 + k_{red}wc \equiv R_x(\mathbf{C}) \\
 \frac{dy}{dt} &= -k_1xy - k_2y - k_5yp + k_6u + k_7u + k_9z + k(I)\frac{cb}{b_c + b} \equiv R_y(\mathbf{C}) \\
 \frac{dz}{dt} &= k_{red}wc - k_9z - k_{10}z + k(I)\frac{cb}{b_c + b} \equiv R_z(\mathbf{C}) \\
 \frac{dw}{dt} &= 2k_4x - 2k_rw^2 - k_{red}wc \equiv R_w(\mathbf{C}) \\
 \frac{dp}{dt} &= 2k_1xy + k_2y + k_3x^2 - k_5yp + k_6u - k_8p \equiv R_p(\mathbf{C}) \\
 \frac{du}{dt} &= k_5yp - k_6u - k_7u \equiv R_u(\mathbf{C})
 \end{aligned} \tag{1.1}$$

The values for the rate constants and concentrations we use are listed in Table S2. Additional source terms $\propto k(I)$ added to the rate equations for the inhibitor and catalyst include the effect of the light sensitive catalyst $[\text{Ru}(\text{bpy})_3]^{2+}$. While our solution contains both Ferriin and $[\text{Ru}(\text{bpy})_3]^{2+}$ catalysts, we do not make a distinction between them in our model of the system.

Finite Element Model (FEM)

To model the reaction-diffusion front propagation through the linear arrays, we use the finite element software COMSOL to solve the full reaction diffusion equations in two-dimensions

$$\frac{\partial \mathbf{C}}{\partial t} = \mathbf{R}(\mathbf{C}) + D\nabla^2 \mathbf{C} , \tag{1.2}$$

where $\mathbf{C} = \{x \cdots u\}$ and the reactions $\mathbf{R}(\mathbf{C})$ are as stated in Eq. 1.1. At the interface between the aqueous phase and the PDMS a Robin's boundary condition for the Bromine in each phase maintains the partitioning between the phases as follows

$$\begin{aligned} \hat{\mathbf{n}} \cdot D_{u,aq} \nabla u_{aq} &= k(Pu_{aq} - u_p) \Big|_{\partial\Omega_{aq/P}} \\ \hat{\mathbf{n}} \cdot D_{u,p} \nabla u_p &= -k(Pu_{aq} - u_p) \Big|_{\partial\Omega_{aq/P}} \end{aligned} \quad [1.3]$$

The parameter $P \sim 2.5$ is the PDMS - aqueous partition coefficient for bromine and k is a large constant that enforces the partition coefficient while ensuring mass flux continuity across the interface; past simulations⁵ have used values $O(10^4)$, we find that computational times can be reduced by using values $O(10^2)$ without materially altering the solution. The principal assumption here is that the interface is always locally at equilibrium and therefore does not offer any resistance to mass transfer. At the boundaries of the computational domain and at the PDMS - aqueous interface for all other species, the natural no-flux boundary condition $\hat{\mathbf{n}} \cdot D_c \nabla \mathbf{C} = 0 \Big|_{\partial\Omega}$ is used. We used two levels of light inhibition a high value $O(10^{-3})$ in the moat to maintain the constant chemical boundary condition and a lower level $O(10^{-6} - 10^{-5})$ to push the chemistry from the oscillatory regime into the excitable state.

Supplementary Figures

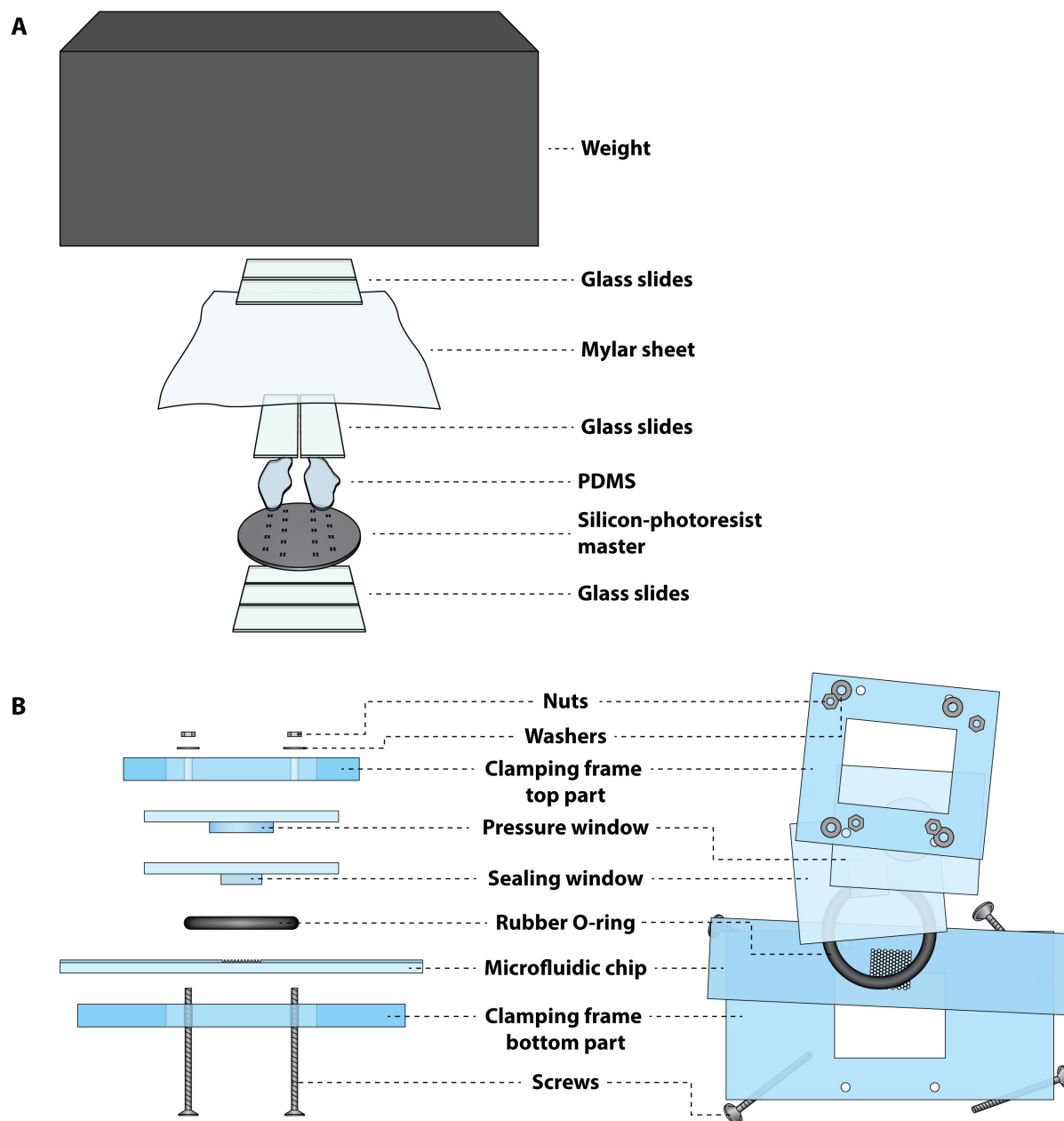


Fig. S1. (A) Schematic of setup for fabricating a thin PDMS microfluidic device. From bottom to top: (1) Three glass slides to provide an even surface. (2) Silicon-photoresist master. (3) PDMS that is poured onto the features of the master. (4) Plasma cleaned glass slides as base of the microfluidic chip. (5) Sheet of Mylar to facilitate disassembly. (6) Glass slides to distribute pressure of weight. (7) 15 kg lead weight. Fabrication process is shown in Movie S6. (B) Experimental Setup. Side view (left) and top view (right)

of disassembled clamping device used for sealing a PDMS chip loaded with BZ solution. From bottom to top: Screws, bottom acrylic glass clamping frame, patterned microfluidic chip, rubber O-ring, sealing glass window, pressure glass window, top acrylic glass clamping frame, washers, screw nuts. Objects are not to scale. For simplification purposes the depicted microfluidic chip contains only one array of wells; the actual microfluidic chips contain 15 sections that can be individually sealed (see Fig. S9). The assembly of the clamping device is shown in Movie S7.

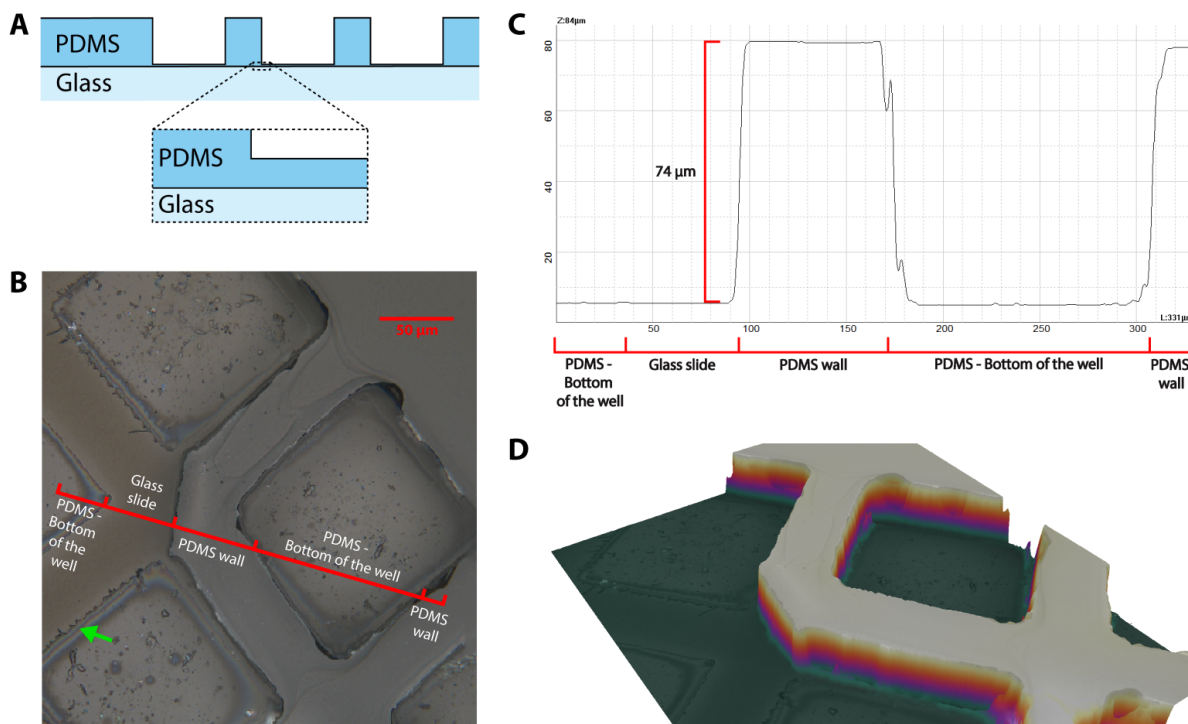


Fig. S2. (A) Section view of microfluidic device. Magnified area illustrates thin layer of PDMS at the bottom of each microfluidic well. (B) Photograph of a microfluidic chip with parts of the PDMS sheet removed with a scalpel: PDMS walls on the left side are missing. The thin layer of PDMS at the bottom of each well remains attached to the glass. Interference fringes (green arrow) are visible which indicate that the thickness of the PDMS on the bottom of the well is under 1 micron thick. (C and D): Topographical rendering of microfluidic features, with partially removed PDMS layer. (C) 2D profile of the section corresponding to the red line in the top view image shown in (B). PDMS layer at the bottom of wells is too thin to be visible in the profile. (D) Rendered 3D image of the topological scan. Color indicates height.

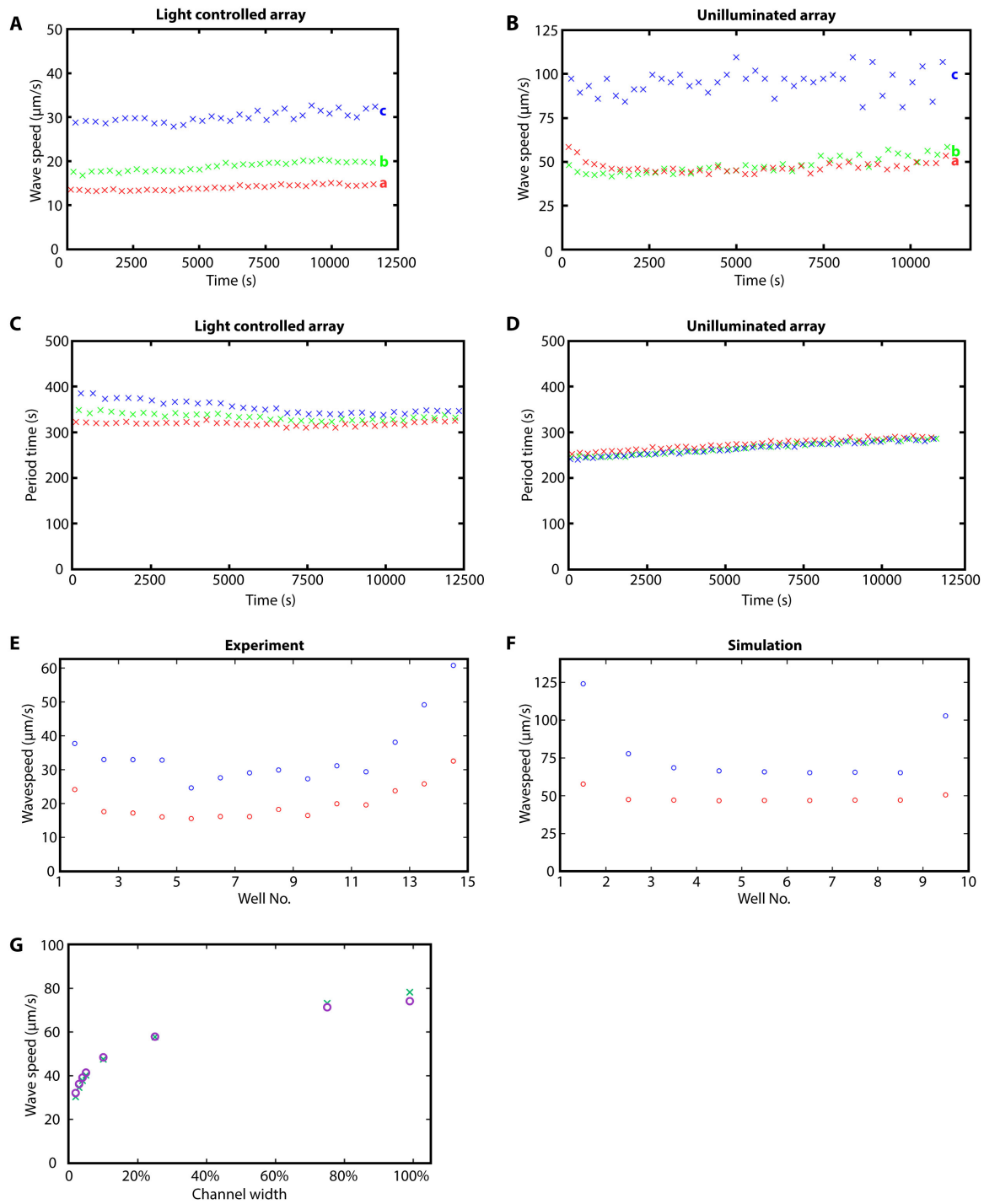


Fig. S4. (A) Propagation speed of waves in the microfluidic design shown in Fig. 4C as a function of time. Each color represents the wave speeds in one of the three columns (Fig. 4C). (a) and (b) are the two geometrically identical arrays, consisting of fifteen wells connected by channels. (c) is a continuous chamber, which can be considered as an array with wells and channels of equal size. Each data point is

the average speed of a single propagating wave. The greatest wave speed is in the continuous channel (c). The difference in wave speeds between (a) and (b) shows typical experimental variances for identical geometries. **(B)** Propagation speed of waves in experiment without controlled pacemaker. As in (A), each data point is the average speed of a single propagating wave and the letters (a), (b) and (c) represent the same columns from the PDMS device shown in Fig. 4C. In contrast to the wave speed plot in (A), here we didn't shine light on the arrays of wells, but only inhibited the BZ filled moat with light. The greatest wave speed is still in the continuous chamber (c), but wave speed is scaled up. **(C and D)**: Period times of oscillations. **(C)** Periods of oscillations of the pacemaker well of each of the three one-dimensional arrays as seen in Fig. 4C over the course of the experiment. Colors of the data points match the colors in (A) and (B). **(D)** Same plot for the experiment without pacemaker wells (B). Shown are the period times in the wells in which the waves originate. **(E and F)**: Spatial dependency of propagation speed. **(E)** Spatial dependency of the propagation speed in experiment with array of wells (design like Fig. 4C). As the chemical wave travels from the first well in the array to the last well, the propagation speed of the wave is not constant. In red is the wave speed of an array of 15 wells with a channel cross section area of 9.5% of the entire cross section of a well. In blue the wave speed of a continuous chamber representing an array of wells with 100% channel cross section area. **(F)** Plotted are the same properties, but from a 2D simulation of the same kind of experiment with 10 wells in a row. In red is the propagation speed of wells that are connected by channels that have 10% of the width of a well; in blue the propagation speed of wells that are connected by channels that have 99% of the width of a well. We found that in experiments and in simulations the wave speed at the beginning and the end of an array is higher compared to regions in between the two. **(G)** 2-D finite element simulations of wave speed vs channel cross section for BZ waves through linear array of wells. Addition to Fig. 6A: Fig. 6A shows simulation accounting for diffusion through PDMS as green line, which is shown here as purple circles. Simulation with no flux conditions are shown as green crosses and show very little difference in wave speed.

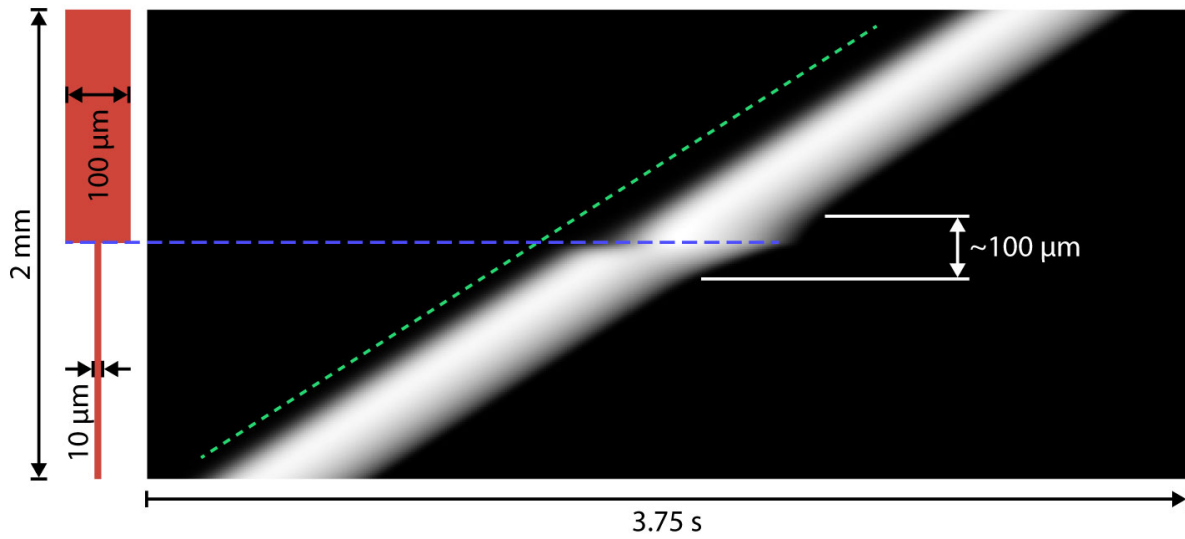


Fig. S5. Space-time plot (right) of FEM predictions showing the propagation of the activator front in a channel with no-flux boundary condition that undergoes a step-change in width (left). The slope of the plot (dashed green line) corresponds to the wave speed. The plot shows that the wave speeds far from the step-change in channel widths are identical, indicating that only the change in width, not the magnitude of the width, determines wave speed. We are also able to garner that the upstream and downstream spatial influence of the step is on the order of the wide channel's dimension, 100 μm.

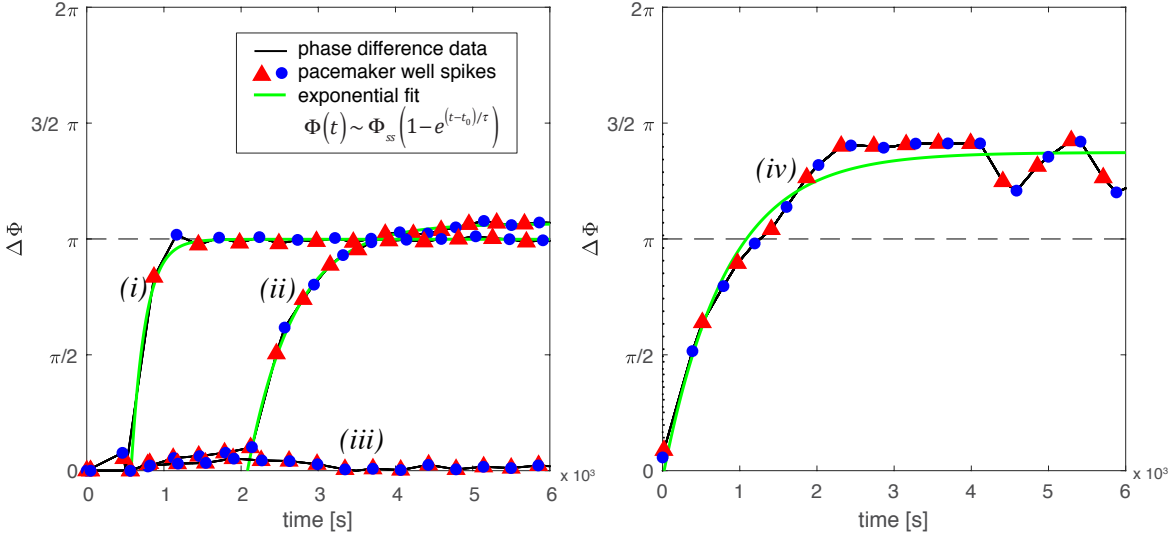


Fig. S6. Phase difference dynamics for four different experiments exhibiting different behaviors: (i) rapid convergence to steady state after a few nearly in-phase oscillations, (ii) slightly slower convergence to steady after multiple in-phase oscillations, (iii) in-phase for the duration of the experiment, and (iv) slow exponential approach immediately after light is removed and convergence to an undesired steady state. In (i) and (ii) only the data after the initial in-phase oscillations have ceased is used for the exponential fit. The dynamics of cases (i) and (ii) exhibit dynamics captured by our finite element analysis (Fig. S8), which also predicts that the lag time depends on coupling strength. Fully characterizing the coupling time experimentally is a task we leave for future work; however, we summarize our current findings in Fig. S7.

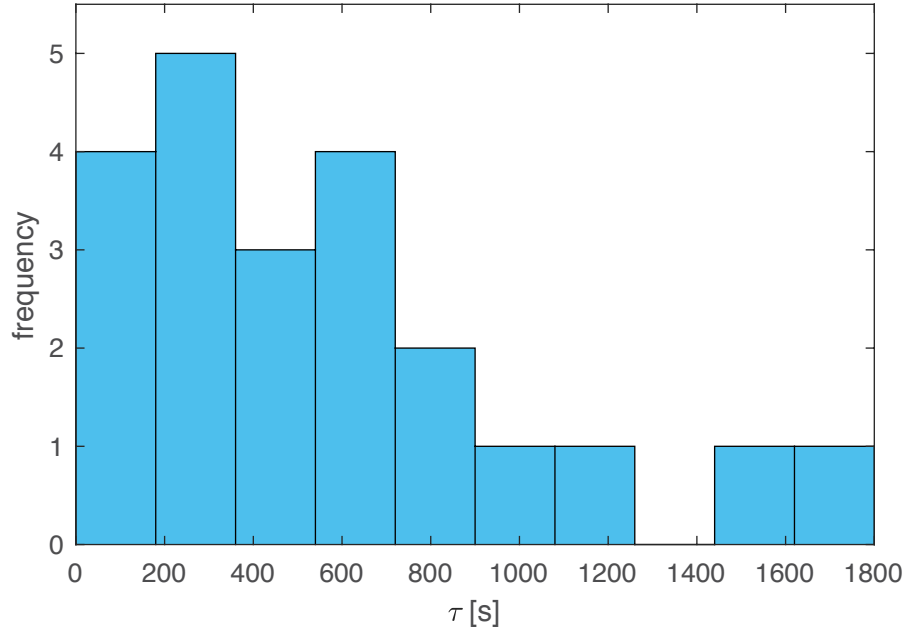


Fig. S7. To characterize the strength of the dynamical attractor, we plot a histogram of coupling time τ measured by fitting an exponential of the form $\Delta\Phi(t) \sim \Delta\Phi_{ss}(1 - e^{-(t-t_0)/\tau})$ to experimental data. Distance between excitatory channels varies from 50 to 70 microns. In-phase oscillations (see Fig. S6) are excluded from the fit. The distribution is peaked around 300 seconds but is broad. For comparison, we explore coupling dynamics over a large range of distances in simulation (Fig. S8) but do not find a broad distribution in the exponential part of the coupling time. We suspect that chip-to-chip variations in the PDMS layer beneath the wells (nominally 1 micron) contributes to the broadness of this distribution; a theory that remains to be tested.

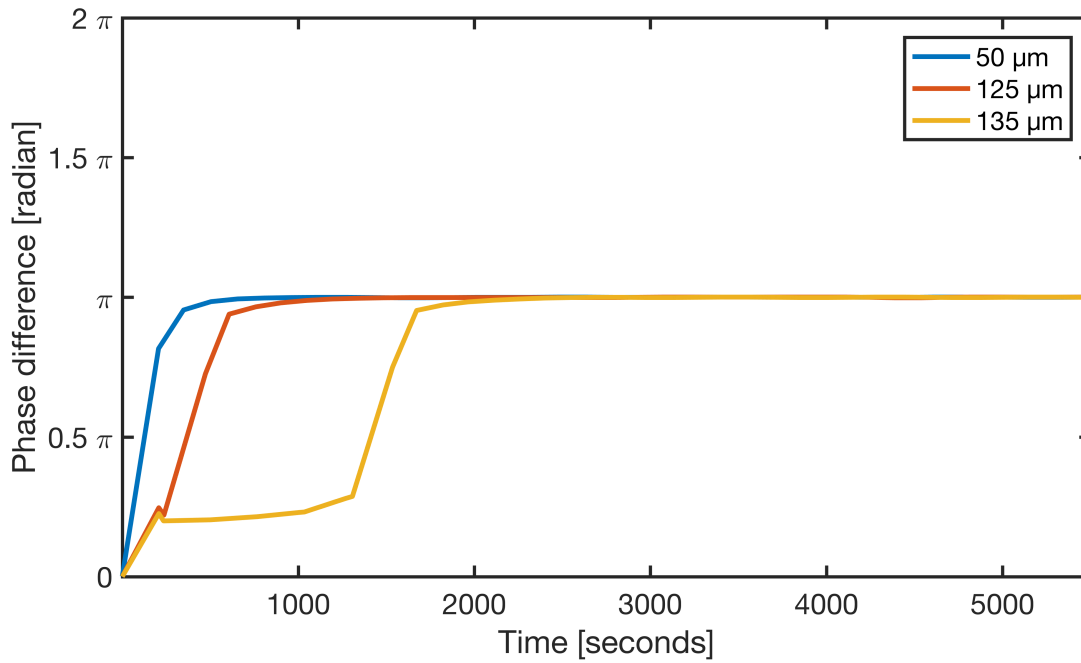


Fig. S8. FEM simulation of BZ-CPGs. Phase difference between the linear arrays vs. time. The two arrays start with pacemakers near in-phase and switch to an anti-phase pattern. Shown is the evolution of phase difference for three different separation distances: 50 μm , 125 μm , and 135 μm . Interestingly, varying the distance increased the lag time while minimally impacting the exponential part of the approach to steady state. Since we were unable to produce the long coupling times ($\tau > 800$ s) observed in experiment, we posit that experimental factors such as the thickness of the PDMS layer beneath the wells impacts dynamics in certain regimes, a hypothesis that would require a full 3D simulation to explore theoretically.

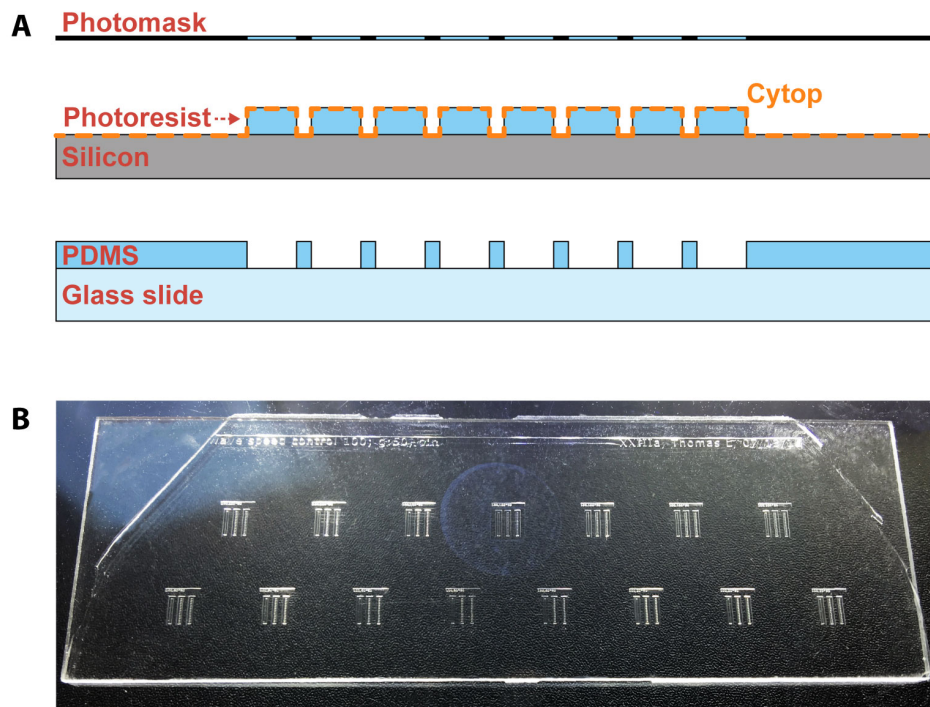


Fig. S9. (A) Illustration of the stages of the fabrication process. From top to bottom: Photomask, silicon-photore resist master and final chip. Structures are not to scale. The fabrication of the silicon-photore resist master and the final microfluidic device are described in the methods section. (B) Photograph of a microfluidic chip. Each chip contains 15 independent devices of which each one can be used in an experiment after being sealed by a 3.2 mm x 3.2 mm glass window. On the depicted chip, each device contains three 1D arrays similar to the ones in Fig. 4C.

Supplementary Tables

Name	Chemical Formula	Final Concentration	Stock Concentration
Malonic Acid	$\text{CH}_2(\text{COOH})_2$	400 mM	2400 mM
Sulfuric Acid	H_2SO_4	80 mM	480 mM
Sodium Bromide	NaBr	25 mM	125 mM
Sodium Bromate	NaBrO_3	288 mM	1728 mM
Ferriin	$\text{C}_{36}\text{H}_{24}\text{FeN}_6^{2+}$	3 mM	18 mM
$[\text{Ru}(\text{bpy})_3]\text{Cl}_2$	$\text{C}_{30}\text{H}_{24}\text{N}_6\text{Cl}_2\text{Ru}\cdot 6\text{H}_2\text{O}$	1.2 mM	7.2 mM

Table S1. BZ reagents. List of BZ reagents with common names, chemical formulas, final concentrations and stock concentrations. To prepare the BZ reaction solution with the stated final concentrations, we mix equal volumes of stock solutions of each reagent with the specified stock concentrations.

Species	Symbol	Value	Rate Constant	Value
$[\text{HBrO}_2]$	x	~	k_1	$2 \times 10^6 [\text{M}^{-2}\text{s}^{-1}]h$
$[\text{Br}_-]$	y	~	k_2	$2 [\text{M}^{-3}\text{s}^{-1}]h^2a$
$[\text{Br}_2]$	u	~	k_3	$3000 [\text{M}^{-1}\text{s}^{-1}]$
$[\text{Fe}(\text{phen})_3^{3+}]$ & $[\text{Ru}(\text{bibpy})_3^{3+}]$	z	~	k_4	$42 [\text{M}^{-2}\text{s}^{-1}]ha$
$[\text{Fe}(\text{phen})_3^{2+}]$ & $[\text{Ru}(\text{bibpy})_3^{2+}]$	c	~	k_5	$5 \times 10^9 [\text{M}^{-2}\text{s}^{-1}]h$
$[\text{BrO}_2^\bullet]$	w	~	k_6	$10 [\text{s}^{-1}]$
$[\text{HOBr}]$	p	~	k_7	$29 [\text{M}^{-1}\text{s}^{-1}]m$
$[\text{H}^+]$	h	160 [mM]	k_8	$9.3 [\text{M}^{-1}\text{s}^{-1}]m$
$[\text{BrO}_3^-]$	a	288 [mM]	k_9	$0.12 [\text{M}^{-1}\text{s}^{-1}]m$
$[\text{CH}_2(\text{COOH})_2]$	m	400 [mM]	k_{10}	$0.05 [\text{M}^{-1}\text{s}^{-1}]m$
$[\text{BrCH}(\text{COOH})_2]$	b	0.12m	k_r	$2 \times 10^8 [\text{M}^{-1}\text{s}^{-1}]$
$[\text{Fe}(\text{phen})]_+$ $[\text{Ru}(\text{bibpy})]$	c_0	4.2 [mM]	k_{red}	$5 \times 10^6 [\text{M}^{-1}\text{s}^{-1}]$

Table S2. BZ species in simulations. Symbol key, reaction rates and constants used in the FKN⁴ (Eq. 1.1).

Supplementary Movies

Movie S1: Waves traveling in three 1D reaction-diffusion geometries are shown. The left and middle arrays consist of fifteen wells connected by channels. The rightmost is a continuous chamber, representing an array with wells and channels of equal size. The rows of wells are surrounded by a large compartment, or “moat”, to establish constant chemical boundary conditions. The moat is filled with BZ solution and illuminated with light to suppress oscillations. The left and middle arrays are identical and consist of fifteen $100\ \mu\text{m} \times 100\ \mu\text{m} \times 110\ \mu\text{m}$ wells connected by channels that are $20\ \mu\text{m}$ wide, $50\ \mu\text{m}$ long and $52\ \mu\text{m}$ deep. The long column on the right is a $100\ \mu\text{m}$ wide, $2200\ \mu\text{m}$ long and $110\ \mu\text{m}$ deep chamber. On the left array, light is shone on all wells except for the well at the bottom. The one uninhibited well acts as a pacemaker. The pacemaker for the middle array is the top well and the pacemaker for the rightmost, continuous channel is located at the bottom. A space time plot of the left array is shown in Fig. 5B.

Movie S2: FEM simulations of wave propagation through a linear array. Wells are $100\ \mu\text{m} \times 100\ \mu\text{m}$, and connected with $80\ \mu\text{m}$ long, $5\ \mu\text{m}$ wide channels. 0:00-0:14: Simulation showing an entire array of 15 wells; color shows the concentration of oxidized catalyst. 0:14-0:28: Close-up with two wells connected by a channel. FEM simulation showing activator concentration (color map), flux (arrows) and the geometry of the wave front (a contour corresponding to half the maximum activator concentration was labeled with a thick, magenta line to help visualize the wave) as it emanates from a small channel.

Movie S3: Experiment like in Movie S1, but with channels that are only $34\ \mu\text{m}$ deep. Half of the waves terminate before reaching the end of the array. A space time plot of this video is shown in Fig. 6C.

Movie S4: Two excitatory coupled linear arrays constructed from PDMS are placed side-by-side and filled with BZ solution. The arrays are surrounded by a moat. All wells are $120\ \mu\text{m} \times 80\ \mu\text{m} \times 90\ \mu\text{m}$. Connecting channels are $50\ \mu\text{m}$ long, $20\ \mu\text{m}$ wide and $40\ \mu\text{m}$ deep. 0:00-0:25: Experiment with a design in which $70\ \mu\text{m}$ of PDMS separates the two linear arrays (shown in Fig. 8 (A to C)). 0:25-2:08: Experiment in which only $50\ \mu\text{m}$ separate the two linear arrays.

Movie S5: FEM simulation of dual channel CPG, color shows the inhibitor (bromine) concentration which drives the columns towards antiphase synchrony. The dimensions of each linear array are the same as those in Movie S2; the columns are separated by $50\ \mu\text{m}$.

Movie S6: Fabrication of a thin PDMS device. See methods section and Fig. S1A.

Movie S7: Loading a PDMS device with the BZ solution and sealing procedure. See methods section and Fig. S1B.

Supplementary References

1. M. Heymann, S. Fraden and D. Kim, *Journal of Microelectromechanical Systems*, 2014, **23**, 424-427.
2. N. Tompkins and S. Fraden, *American Journal of Physics*, 2016, **84**, 150-158.
3. N. Tompkins, N. Li, C. Girabawe, M. Heymann, G. B. Ermentrout, I. R. Epstein and S. Fraden, *Proc Natl Acad Sci U S A*, 2014, **111**, 4397-4402.
4. R. M. Noyes, R. Field and E. Koros, *Journal of the American Chemical Society*, 1972, **94**, 1394-1395.
5. V. Horvath, D. J. Kutner, J. T. Chavis Iii and I. R. Epstein, *Physical Chemistry Chemical Physics*, 2015, **17**, 4664-4676.